ACS APPLIED MATERIALS & INTERFACES

Research Article

www.acsami.org

p–i–n Heterojunctions with $BiFeO_3$ Perovskite Nanoparticles and p- and n-Type Oxides: Photovoltaic Properties

Soumyo Chatterjee, Abhijit Bera, and Amlan J. Pal*

Department of Solid State Physics, Indian Association for the Cultivation of Science, Jadavpur, Kolkata 700032, India

Supporting Information

ABSTRACT: We formed p–i–n heterojunctions based on a thin film of $BiFeO_3$ nanoparticles. The perovskite acting as an intrinsic semiconductor was sandwiched between a p-type and an n-type oxide semiconductor as hole- and electron-collecting layer, respectively, making the heterojunction act as an all-inorganic oxide p–i–n device. We have characterized the perovskite and carrier collecting materials, such as NiO and MoO_3 nanoparticles as p-type materials and ZnO nanoparticles as the n-type material, with scanning tunneling spectroscopy; from the spectrum of the density of states, we could locate the band edges to infer the nature of the active semiconductor materials. The energy level diagram of p–i–n heterojunctions showed that type-II band alignment formed at the p–i and i–n interfaces, favoring carrier separation at both of them. We have compared the photovoltaic properties of the perovskite in p–i–n heterojunctions and also in p–i and i–n junctions. From current–voltage characteristics and impedance spectroscopy, we have observed that two depletion regions were formed at the p–i and i–n interfaces of a p–i–n heterojunction. The two depletion regions operative at p–i–n heterojunctions have yielded better photovoltaic properties as compared to devices having one depletion region in the p–i or the i–n junction. The results evidenced photovoltaic devices based on all-inorganic oxide, nontoxic, and perovskite materials.

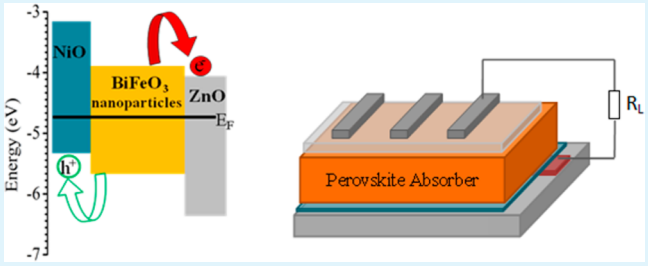

KEYWORDS: *$BiFeO_3$ nanoparticles, perovskites, NiO, MoO_3 and ZnO nanoparticles, p–i–n heterojunctions, photovoltaic properties of all oxide p–i–n heterojunctions*

INTRODUCTION

In research beyond silicon solar cells, a range of direct band gap materials has been considered in recent years.[1−3] One of the most important advantages of using direct band gap semiconductors is that the thickness of the active materials could be minimized to reduce the internal resistance of the cells. Ideally, in a bilayer structure, the total thickness of the active layer should be the sum of the width of the depletion region and the diffusion length of carriers at the two sides of the region, so that all the photogenerated excitations can contribute to photocurrent.[4−7] The device architectures that have been considered in this direction are p–n and p–i–n junctions apart from the conventional Schottky devices as an example of single layer device structure.[6−10] In p–i–n junctions, an intrinsic semiconductor acting as an absorber layer is sandwiched between p- and n-type layers, so that the depletion regions at the p–i and i–n are added up and an internal field is formed across the entire layer of the intrinsic semiconductor material. An open-circuit voltage (V_{OC}) and a short-circuit current (I_{SC}) are generated due to a separation of photogenerated charge carriers by the internal depolarization electric field.

The class of intrinsic semiconductors that is being considered as an absorber material is perovskites having a $A^{2+}B^{4+}X_3^{2-}$ structure.[11−14] A similar perovskite material based on organic and inorganic hybrid moieties, namely, methylammonium lead iodide $[(CH_3NH_3)^+Pb^{2+}I_3^-]$, has further expedited research in this direction due to the increased power conversion efficiency of such solar cells.[15−17] TiO_2 as an electron-transport layer and a suitable hole-transport layer (mostly a derivative of spirobifluorene) are commonly used as n- and p-type materials, respectively; indium tin oxide (ITO) and gold acted as the electron- and hole-collecting electrodes, respectively. The n–i–p heterojunctions have been termed as an inverted device structure.

The success of $(CH_3NH_3)^+Pb^{2+}I_3^-$, which is a hybrid perovskite containing organic groups, has however not deterred the quest for inorganic perovskite oxides. Inorganic perovskites, which are highly stable, can furthermore be based on nontoxic elements, the use of which is a prerequisite for device applications. In this direction, bismuth ferrite ($BiFeO_3$) is one of the few multiferroics that has its both Curie and Néel temperatures above room temperature.[18] With a direct band gap of 2.2–2.8 eV, this material can respond well to photons to generate a steady-state photocurrent under the effect of an internal electric field.[18,19] In this direction, the photovoltage in $BiFeO_3$ appeared due to its domain-wall boundaries, loss of inversion symmetry in the distribution of defects, impurities, space charges, and a higher saturation polarization ef-

Received: September 5, 2014
Accepted: October 28, 2014
Published: October 28, 2014

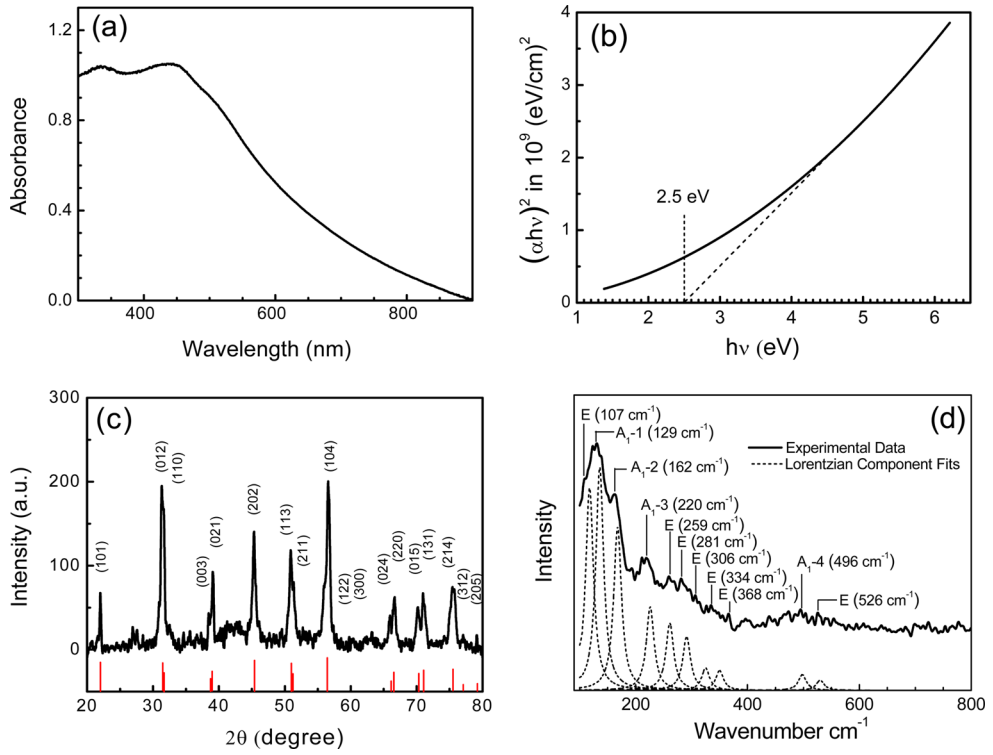

Figure 1. Characteristics of $BiFeO_3$ nanoparticles: (a) optical absorption spectrum; (b) a plot of $(\alpha h\nu)^2$ versus energy, with the broken line being used to determine the band gap of the nanoparticles; (c) XRD analysis; and (d) Raman spectrum with peaks fitting to individual Lorentzian components.

fect.[18,20−22] In $BiFeO_3$ thin films, domain walls ranging between 10 and 100 in number are electrically connected in series; an electric field generated in the domains drives the photogenerated charge carriers opposite to the domain boundaries, thereby providing a drift current. These carriers recombine with charge carriers of the neighboring domain-walls and hence reduce the concentration of opposite charge carriers and thereby in turn decrease the photocurrent. A reduction in the recombination rate at the adjacent domain walls will hence lead to an increased diffusion current. While most of the photovoltaic studies of $BiFeO_3$ are based on its thin-film form,[23−26] a singular work accounted for nanoparticles of the perovskite in a conjugated polymer matrix in forming hybrid bulk-heterojunction solar cells.[27]

In this work, we have used $BiFeO_3$ nanoparticles as an absorber. Inorganic oxides, such as either NiO or MoO_3 as a p-type hole-collecting layer and n-type ZnO as an electron-collecting layer, have been used along with the perovskite to form an all-inorganic p−i−n direct device structure based on oxides of nontoxic elements to study the photovoltaic properties.

EXPERIMENTAL SECTION

Growth of $BiFeO_3$ Nanoparticles. Bismuth(III) nitrate pentahydrate [$Bi(NO_3)_3{\cdot}5H_2O$] and iron(III) nitrate nonahydrate [$Fe(NO_3)_3{\cdot}9H_2O$] purchased from Sigma-Aldrich Co. were used for the growth of $BiFeO_3$ nanoparticles. To do so, we have followed a reported sol−gel reaction route in which equimolar amounts (0.01 M) of the nitrates were added to 12 mL of ethylene glycol in succession.[28] The contents were stirred until a clear reddish solution was formed. The solution was then warmed to 80 °C until the entire fluid evaporated to leave a light-yellow gel. The temperature of the content was further raised to 300 °C at a rate of 5 °C/min to remove the excess hydrocarbon- and nitrogen-based impurities. The as-obtained solid was calcinated at 320 °C for 30 min to obtain a reddish-brown and strongly magnetic $BiFeO_3$ powder, which was ground in a mortar for a while. The nanoparticles were dissolved in HPLC-grade methanol, sifted through a syringe filter, and redissolved for further use.

Growth of MoO_3 and ZnO Nanoparticles and NiO Layer. The commonly used nanoparticles were grown through reported colloidal synthesis routes,[29,30] the details of which are described in the Supporting Information. The reported method[31] followed to form the NiO layer is also described in the Supporting Information.

Characterization of the Nanoparticles. The as-prepared nanoparticles were characterized by optical absorption spectroscopy, Raman spectroscopy, X-ray diffraction (XRD) patterns, scanning electron microscopy (SEM), atomic force microscopy (AFM), energy-dispersive X-ray (EDX) analysis, transmission electron microscopy (TEM), and high-resolution TEM (HR-TEM). The measurements were carried out with a Shimadzu UV-2550 spectrophotometer, a Horiba Jobin-Yvon Raman triple grating spectrometer system (model number T64000) using 514 nm excitation of a Spectra Physics laser source (model number Stabilite 2017), a Bruker D8 Advanced X-ray powder diffractometer, a JEOL JSM 6700F field emission SEM, a Nanosurf Easyscan2 AFM, and a JEM 2100F JEOL TEM, respectively. To locate the conduction and valence band edges of $BiFeO_3$ nanoparticles, the tunneling current of an ultrathin film of the nanocrystals was recorded with a Nanosurf Easyscan2 scanning tunneling microscope (STM) under ambient conditions. The density of states (DOS) of the nanocrystals enabled us to locate the band edges of the semiconductors with respect to the Fermi energy.[32] For STM measurements, voltage was applied with respect to the substrate electrode.

Device Fabrication. All-inorganic p−i−n direct device structures were fabricated on patterned indium tin oxide (ITO)-coated glass substrates (width = 2 mm) having a surface resistance of 15 Ω/square. The ITO substrates were cleaned following a usual protocol. They were further treated with ozone to achieve a better contact with the active layer by reducing the contact resistance. To fabricate the devices, a layer of either NiO or MoO_3 nanoparticles as p-type hole-

collecting material, a layer of $BiFeO_3$ nanoparticles as an absorber, and another layer of n-type ZnO as an electron-collecting material were formed in sequence. To obtain a layer of NiO, $Ni(OH)_2$ solution was spun at 3000 rpm for 30 s followed by annealing of the film at 425 °C for 10 min in an oxygen environment. For devices with MoO_3 nanoparticles in the hole-transport layer, a dispersed solution of MoO_3 nanoparticles in chloroform (15 mg/mL) was spun at 2000 rpm for 30 s followed by annealing at 130 °C for 15 min also in the presence of oxygen. Either of the processes was repeated to obtain a desired thickness of the hole-transport layer (~20 nm). A thin film of sensitizing $BiFeO_3$ nanoparticles was then spun on the hole-transport layer at 2500 rpm for 30 s from a 20 mg/mL methanol solution of the perovskite. The thin film of $BiFeO_3$ nanoparticles was annealed at 150 °C for 20 min in an oxygen environment. The process of film formation was repeated about eight times to obtain a desired thickness of ~600 nm. An electron-transport layer in the form of a layer of ZnO nanoparticles was then spun at 3000 rpm for 30 s from a 6 mg/mL solution of the nanoparticles followed by annealing of the film at 100 °C for 10 min. The deposition of ZnO layer was also repeated to obtain a suitable thickness of the electron-transport layer (~50 nm). As for the top electrode, aluminum was thermally evaporated under vacuum in the form of 2 mm wide strips orthogonal to the ITO ones. Metal deposition was carried out at a rate of 1 Å/s at a pressure lower than 5×10^{-6} Torr until a film thickness of 100 nm was achieved. This completed the device fabrication process with the active area of each cell being 4 mm^2.

Characterization of the Devices. To characterize the photovoltaic devices, they were kept in a shielded vacuum chamber fitted with a quartz window. Current−voltage (I−V) characteristics under a dark and an illuminated condition were recorded with a Keithley 2636 Electrometer using LabTracer software. A 150 W Newport-Stratfort Solar Simulator (model 76500), attached with an AM1.5G filter, acted as the source for illumination. The intensity of the simulated solar light was 100 mW/cm^2. To record the external quantum efficiency (EQE) spectrum of the devices, a Jobin-Yvon H20 monochromator was used to disperse the solar illumination.

Impedance spectroscopy of the sandwiched structures was recorded with a Solartron 1260A impedance analyzer with 10 mV rms as the test ac voltage. The real and imaginary components of complex impedance without any dc bias were recorded by varying the frequency of the ac test voltage in the 0.1 Hz to 10 MHz region (10 points/decade). The impedance analyzer was operated with SMaRT software via a general-purpose interface bus (GPIB).

RESULT AND DISCUSSION

Characterization of the Nanoparticles. The characteristics of MoO_3 nanoparticles, thin films of NiO, and ZnO nanoparticles, as presented in Figures S1−S3 in the Supporting Information, confirmed their formation. Optical absorption, XRD spectra, TEM images, and EDX analyses that matched the reported results are shown as figures.

We have characterized the $BiFeO_3$ nanoparticles in depth. The optical absorption spectrum of the nanoparticles in dispersed solution, as presented in Figure 1a, shows bands at 333 and 439 nm with a continuum extending to the long-wavelength region. The spectrum, which matched the reported results, has also been shown as a plot of $(\alpha h\nu)^2$ versus energy to obtain the optical band gap of the nanoparticles. From the slope of the Tauc plot, as presented in Figure 1b, the band gap could be estimated to 2.5 ± 0.05 eV. The value matches well with the literature;[33] we may also state that the band gap of $BiFeO_3$ is known to depend on the fabrication procedure.[21] XRD analysis of the nanocrystals is presented in Figure 1c. The peaks corresponding to the rhombohedral phase of the perovskite match well with the JCPDS File #20-0169. For further characterization, we have recorded Raman spectrum of the nanomaterial in the form of a pressed palette. The Raman peaks, as shown in Figure 1d, corresponding to A_1 and E modes of the rhombohedral phase with $R3c$ structure, match well with the reported results.[34] The spectrum moreover shows that most of the 13 Raman modes ($4A_1$ + 9E) predicted by group theory of the structure could be fitted to individual Lorentzian components.[35]

A TEM and a HR-TEM image of the nanocrystals are shown in Figure 2. In the TEM image, hexagonal-shaped $BiFeO_3$

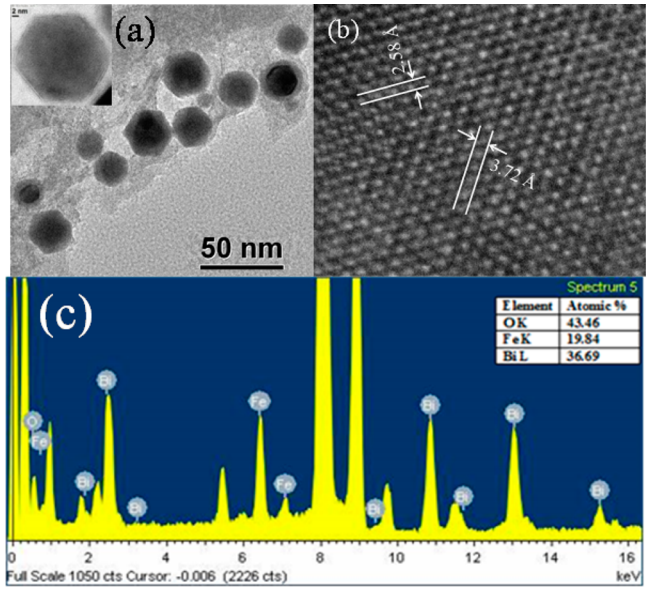

Figure 2. (a) TEM and (b) HR-TEM images and (c) EDX patterns of $BiFeO_3$ nanocrystals along with the atomic percentages of the elements in the material. The inset of part a shows a closeup TEM image of one particle.

nanoparticles having a diameter of 20−25 nm are visible. A HR-TEM image, presented in Figure 2b, shows a typical crystalline domain with an interplanar spacing of 3.72 and 2.58 Å, which match well with the spacing of {101} and {012} planes, respectively, of the rhombohedral phase of $BiFeO_3$ crystal (JCPDS File #20-0169). The composition of the $BiFeO_3$ nanoparticles has been analyzed by EDX; the table presented with Figure 2c shows the atomic percentage of the elements, confirming the composition of the nanocrystals.

Valence state information and elemental composition of $BiFeO_3$ nanocrystals were studied by XPS analysis. A full scan spectrum of the nanocrystals is shown in Figure 3. The spectrum shows the presence of Bi 4d, Bi 4f, Fe 2p, and O 1s peaks, confirming occurrence of the elements in the nanomaterial. We have also recorded a high-resolution spectrum in small energy regions around each of the peaks. As can be observed in Figure 3b, the spectrum resolved the Bi 4d state into $4d_{3/2}$ and $4d_{5/2}$ peaks at 475.5 and 452.0 eV. The Bi 4f similarly resolved into $4f_{5/2}$ and $4f_{7/2}$ peaks at 164.8 and 159.8 eV, respectively. Figure 3c shows that the spectrum for Fe 2p resolved into 711.6 and 724.8 eV peaks that corresponded to $2p_{3/2}$ and $2p_{1/2}$ states, respectively. These energy positions are in concurrence with the reported XPS spectrum of Bi^{3+} and of Fe^{3+}, respectively.[36] Figure 3d shows that the spectrum corresponding to oxygen appeared at 531.3 eV, indicating the existence of the O 1s state of O^{2-}. The spectrum of the O 1s state could be fitted to a symmetric Gaussian distribution with peaks at 529.1 and 532.4 eV.[37,38] The peak at the lower binding

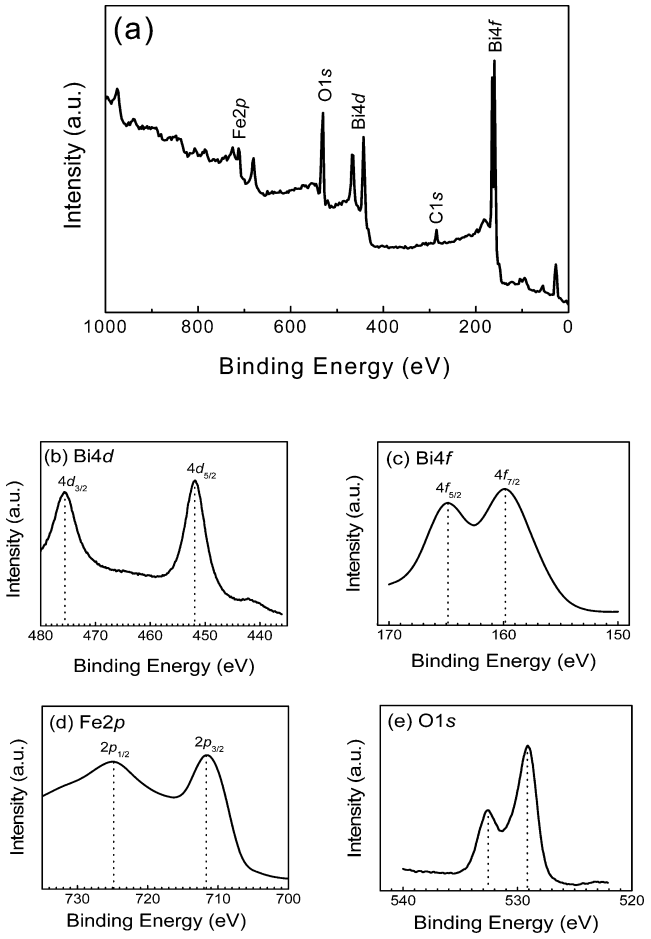

Figure 3. (a) Full-range XPS spectrum of $BiFeO_3$ nanocrystals. High-resolution XPS spectra of (b) Bi 4d, (c) Bi 4f, (d) Fe 2p, and (e) O 1s are shown.

energy corresponded to the core spectrum of O 1s; the higher energy one appeared due to an oxygen-deficient region of the perovskite nanocrystals. The results hence inferred that $Bi^{3+}Fe^{3+}O_3^{2-}$ formed in the nanocrystals.

Optical Absorption of the p–i–n Heterojunction. As we stated, we formed layers of p-type, intrinsic, and n-type semiconductors in sequence to form p–i–n direct structures. While either NiO or MoO_3 nanoparticles were used in forming a p-type layer, $BiFeO_3$ and ZnO nanoparticles formed the intrinsic and n-type semiconductor layer, respectively. To know the spectral window of such a device (NiO–$BiFeO_3$–ZnO), we show optical absorption spectra of the thin films during the stages of the film-deposition process (Figure 4). Absorbance at wavelength regions relevant to each material grew as the layers were deposited. The p–i–n layer absorbed most of the solar spectrum. Uniformity and transparency of the thin film that contained layers of NiO, $BiFeO_3$, and ZnO nanoparticles were of superior quality with few scattering centers (inset of Figure 4). Such films were hence appropriate to study photovoltaic properties. The MoO_3–$BiFeO_3$–ZnO p–i–n thin films returned similar results. The thickness of the layers in the p–i–n heterojunction was measured by recording SEM images in a cross-sectional mode (Figure S4 in the Supporting Information). The thickness of NiO, $BiFeO_3$, and ZnO layers turned out to be 20, 600, and 50 nm, respectively. In addition, the surface profile of p–i–n thin films was imaged with an AFM. Such a topography, along with another for a thin film of

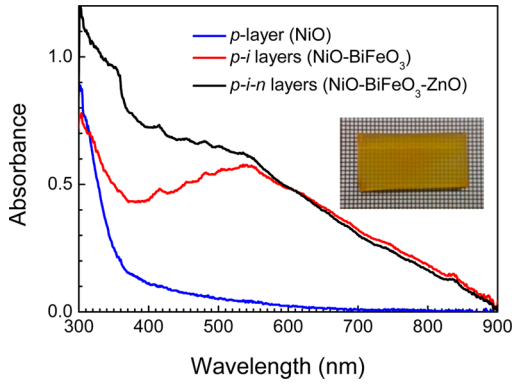

Figure 4. Optical absorption spectra of NiO layer and NiO–$BiFeO_3$ and NiO–$BiFeO_3$–ZnO heterojunctions. A photograph of a NiO–$BiFeO_3$–ZnO heterojunction is shown in the inset.

$BiFeO_3$ nanoparticles, as presented in Figure S5 in the Supporting Information, shows that the thin films were uniform to fabricate sandwiched structures.

Scanning Tunneling Spectroscopy (STS). To know if NiO–$BiFeO_3$–ZnO and MoO_3–$BiFeO_3$–ZnO truly formed a p–i–n configuration with type-II band alignment at the two interfaces, we aimed to locate the conduction and valence band edge of the individual materials. To do so, we recorded tunneling current versus tip voltage characteristics of ultrathin films of the materials formed separately. From the tunneling current, which were nonlinear in nature, we calculated the density of states (DOS) of NiO thin films and MoO_3, $BiFeO_3$, and ZnO nanoparticles (Figure 5). For each of the semiconductors, we recorded the tunneling current at many different points on the ultrathin film. With the tip voltage being applied with respect to the substrate, the peaks in the DOS spectra enabled us to locate the conduction and valence band edges of the semiconductors with the work function of the substrate being aligned to the Fermi energy of the semiconductor. At a positive voltage, the tip withdrew electrons from the semiconductor; similarly, electrons were injected at negative voltages. The peaks (in the DOS spectrum) in the positive and in the negative voltages denoted the location of the valence and conduction bands, respectively, of the semiconductor. The DOS spectra show that the Fermi energy was closer to the valence band edge of NiO and MoO_3, implying the p-type nature of the materials. Similarly, the ZnO nanocrystals acted as an n-type semiconductor. The DOS spectrum of $BiFeO_3$ nanoparticles, as presented in Figure 5c, shows that the perovskite behaved as an intrinsic semiconductor with its Fermi energy being located midway between the band edges.

The results show that the transport gap of $BiFeO_3$ nanocrystals was 1.8 eV, which is expectedly lower than the optical gap of the material, since trap states also contribute to tunneling current and hence appear in the DOS spectrum. The values of band edges of NiO, MoO_3, $BiFeO_3$, and ZnO nanoparticles moreover show that both NiO–$BiFeO_3$–ZnO and MoO_3–$BiFeO_3$–ZnO heterojunctions would form p–i–n structures with type-II band alignment at both the interfaces. In parts e and f of Figure 5, we show the energy band diagram of the two heterojunctions with ITO and aluminum acting as a hole- and an electron-collecting electrode, respectively. The energy levels of the p–i–n structures show that a depletion region would form at the p–i and i–n interfaces of both the

dx.doi.org/10.1021/am506066m | ACS Appl. Mater. Interfaces 2014, 6, 20479–20486

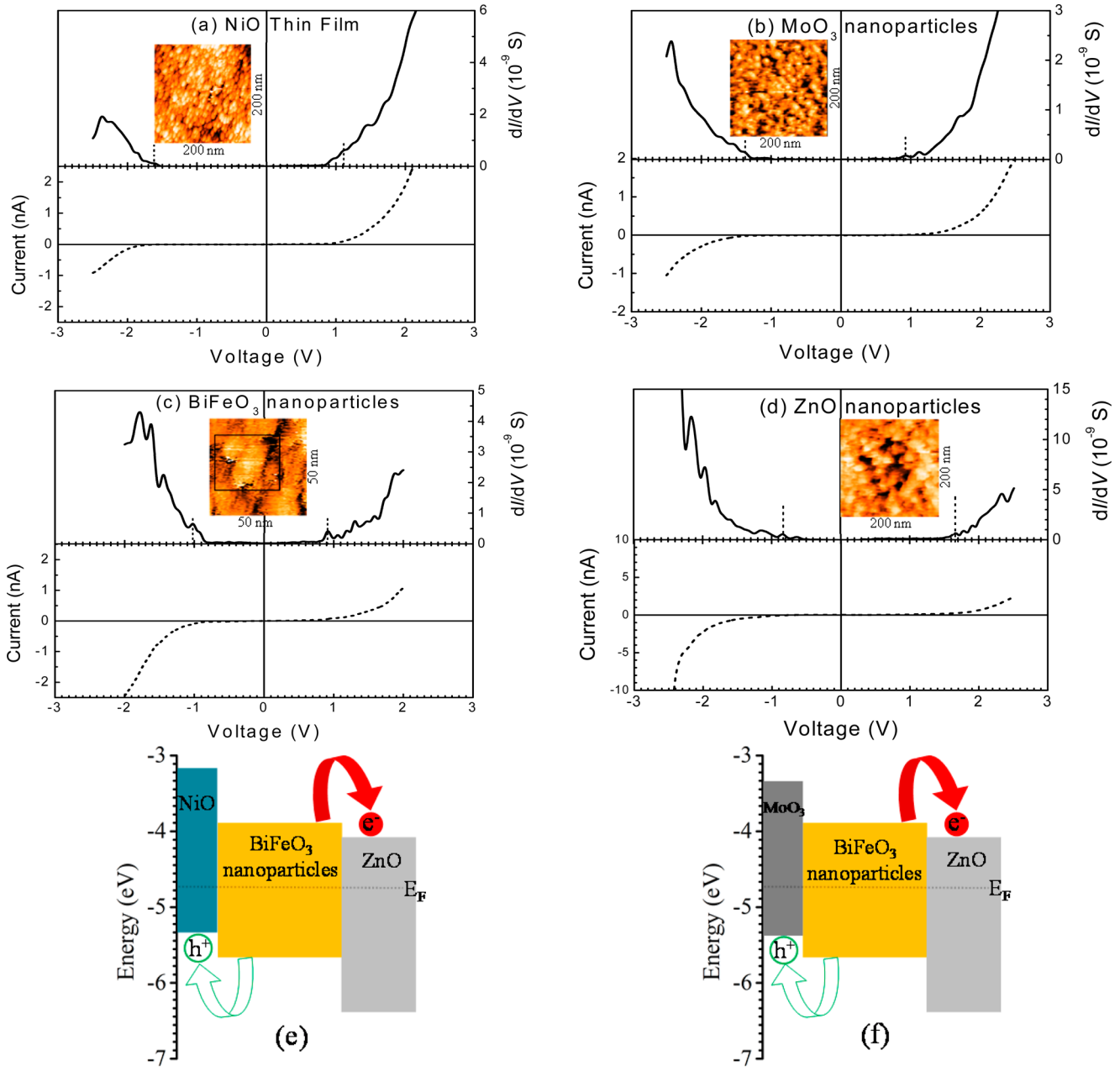

Figure 5. Current–voltage and density of states (dI/dV) plots of (a) NiO thin film and (b) MoO_3, (c) $BiFeO_3$, and (d) ZnO nanoparticles. STM topography of the active layer is shown in the inset of each figure. Schematic descriptions of the energy level diagram of (e) NiO–$BiFeO_3$–ZnO and (f) MoO_3–$BiFeO_3$–ZnO heterojunctions are shown.

heterojunctions. The electrodes' work functions would allow seamless extraction of holes and electrodes without any barriers.

Current–Voltage Characteristics. Current–voltage characteristics of the two p–i–n devices under a dark and an illuminated condition are shown in Figure 6. Both the dark characteristics are rectifying in nature, implying that the device would exhibit photovoltaic properties under illumination. Indeed, under white light illumination, the I–V characteristics showed photovoltaic characteristics typical of a direct structure. The open-circuit voltage (V_{OC}), short-circuit current (I_{SC}), fill factor, and power conversion efficiency (η) of the devices are listed in Table 1. The device with NiO in forming a p-type layer yielded a better I_{SC} and η as compared to the other device that had MoO_3 nanoparticles as the hole-transport layer.

We varied the intensity of illumination while recording photovoltaic properties. Characteristics of NiO–$BiFeO_3$–ZnO heterojunction under white light illumination of different intensities are summed up in Figure 6b. While the I_{SC} expectedly increased with the intensity, the change in V_{OC} was marginal. The power conversion efficiency, on the other hand, showed a higher value at a low illumination intensity, primarily due to a favorable fill factor at a lower illumination condition. The value of η was higher that the reported results from devices based on $BiFeO_3$ thin films or bilayer structures of $BiFeO_3$ with other materials, such as conjugated polymers, graphenes, or other semiconductors.[27,39,40]

It is imperative to compare the p–i–n devices with p–i and i–n devices apart from a single layer device with only the perovskite layer. I–V characteristics of such devices under

dx.doi.org/10.1021/am506066m | ACS Appl. Mater. Interfaces 2014, 6, 20479–20486

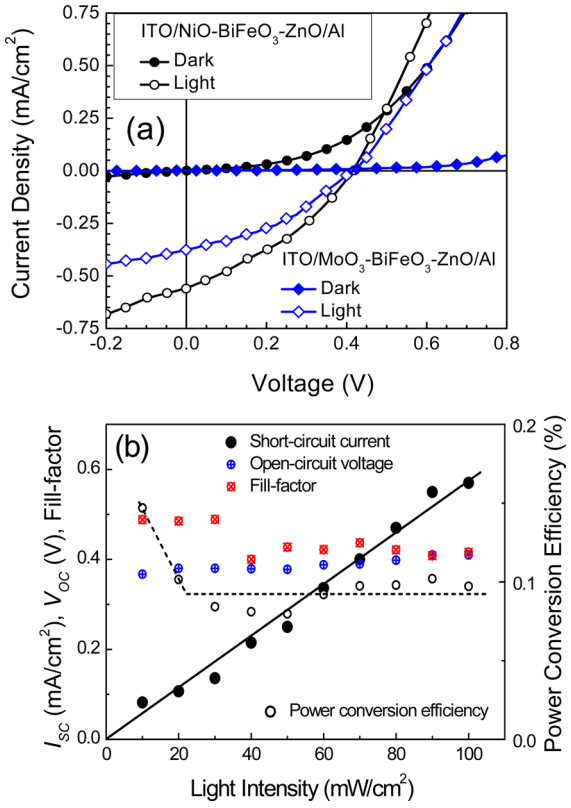

Figure 6. (a) Current–voltage characteristics of NiO–$BiFeO_3$–ZnO and MoO_3–$BiFeO_3$–ZnO heterojunctions under dark and white light illuminated conditions. (b) Plots of I_{SC}, V_{OC}, fill factor, and power conversation efficiency of a device based on NiO–$BiFeO_3$–ZnO heterojunction as a function of the intensity of while light.

illumination are shown in Figure 7. Results from both the hole-transport layers have been included in the figure. A comparison of Figures 6 and 7 shows that the photovoltaic properties of p–i–n devices were superior to the those of other devices. The parameters of p–i, i–n, and the single layer devices have been appended in Table 1. The photovoltaic parameters of p–i–n devices, as also shown in Table 1, are far better than those based on the components of p–i–n devices. The results hence infer that two depletion regions of the p–i–n heterostructure (operative at the p–i and i–n interfaces) together might have brought out favorable photovoltaic properties in the $BiFeO_3$ nanocrystals. It may be stated here that the superiority of the p–i–n device over p–i and i–n ones cannot be solely due to additional photoabsorption in the n- or in the p-layer in the respective device, as evidenced from optical absorption spectra of the layers (Figure 4).

To know if excitons generated in all the layers of p–i–n heterojunction contributed to photocurrent, we recorded the

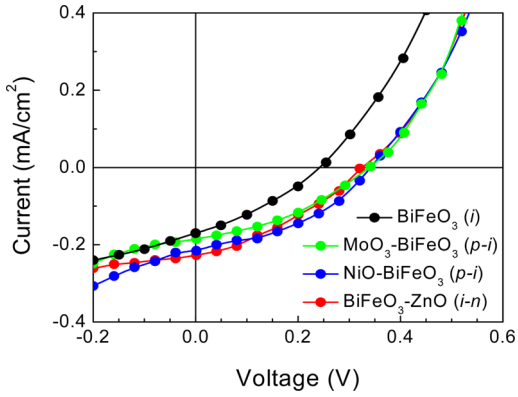

Figure 7. Current–voltage characteristics of different layers or heterojunctions of the p–i–n device, as stated in the legend, under 100 mW/cm^2 white light illumination. ITO and Al electrodes were used to sandwich the active layer(s) of the devices.

external quantum efficiency (EQE) spectrum of the devices. The EQE spectrum of a sandwich structure with NiO–$BiFeO_3$–ZnO heterojunction as the active material is shown in Figure 8. For comparison, we have added the optical absorption

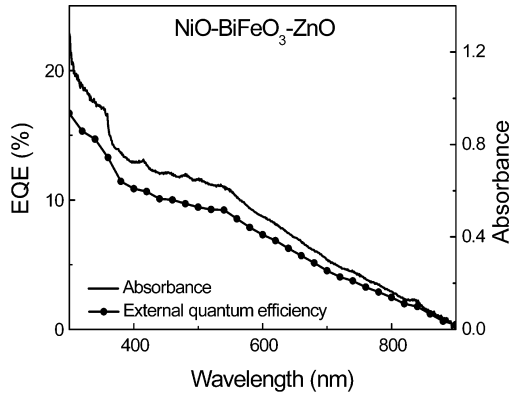

Figure 8. External quantum efficiency (EQE) of NiO–$BiFeO_3$–ZnO (p–i–n) heterojunction sandwiched between ITO and aluminum electrodes and an optical absorption spectrum of the p–i–n heterojunction.

spectrum of the heterojunction. The spectral response of EQE and optical absorption matched well, implying that the excitons generated in the NiO, $BiFeO_3$, and ZnO layers contributed to photocurrent. The EQE spectrum of MoO_3–$BiFeO_3$–ZnO heterojunction similarly matched the optical absorption spectrum of the active layer (Figure S6 in the Supporting Information). The results hence infer that depletion regions must have formed at both p–i and i–n junctions, so that all three layers of the p–i–n heterojunction could contribute to

Table 1. Photovoltaic Properties of Different Heterojunctions (p–i, i–n, and p–i–n) and $BiFeO_3$ Layer Sandwiched between ITO and Al Electrodes, As Derived from Figures 6 and 7

active layer	abbrev	V_{OC} (V)	I_{SC} (mA/cm^2)	fill factor (%)	% power conversion efficiency (η) at 1 sun
$BiFeO_3$	i	0.24	0.17	31.8	1.3×10^{-2}
MoO_3–$BiFeO_3$	p–i	0.33	0.18	36.8	2.2×10^{-2}
NiO–$BiFeO_3$		0.34	0.21	40.3	2.9×10^{-2}
$BiFeO_3$–ZnO	i–n	0.32	0.23	33.5	2.5×10^{-2}
MoO_3–$BiFeO_3$–ZnO	p–i–n	0.42	0.38	35.7	5.7×10^{-2}
NiO–$BiFeO_3$–ZnO		0.41	0.57	41.8	9.8×10^{-2}

dx.doi.org/10.1021/am506066m | ACS Appl. Mater. Interfaces 2014, 6, 20479–20486

yield photocurrent through diffusion of carriers through the depletion regions.

Impedance Spectroscopy. To obtain further insights on the depletion regions in p−i−n devices that would form a capacitive component of complex impedance of the sandwiched structure, we have recorded impedance spectroscopy of the devices under a dark and an illuminated condition. Nyquist plots of a NiO−$BiFeO_3$−ZnO (p−i−n) device in the dark and with illumination are shown in Figure 9. No dc bias was applied

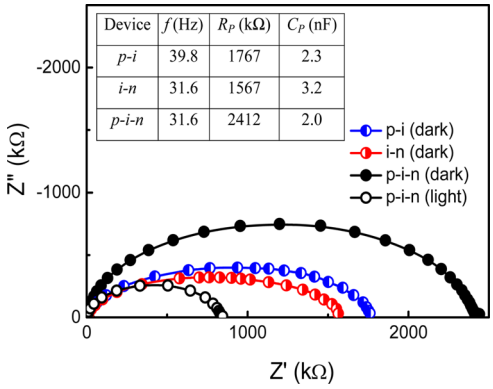

Figure 9. Plots of the real and imaginary components of the complex impedance of NiO−$BiFeO_3$−ZnO (p−i−n), p−i, and i−n heterojunction under a dark condition. For the p−i−n device, the plot under 100 mW/cm^2 white light illumination is also shown in the figure. ITO and Al electrodes were used to sandwich the active layers to form devices. Inset of the figure shows the R_P, the frequency at the apex of Nyquist plots (f), and the corresponding C_P of the C_P−R_P electrical analogue of different devices under a dark condition.

during the measurements. The plots are semicircular in nature, suggesting that the devices could be modeled to a combination of a resistor and a capacitor in parallel configuration (C_P−R_P). The diameter of the semicircle with the abscissa represents the bulk resistance (R_P) of the device. The plots show that the bulk resistance decreased upon illumination. The sharp decrease in device resistance under illumination has occurred due to generation of free carriers upon exciton dissociation in the device. Since the frequency at the apex of a Nyquist plot represents a characteristic angular frequency (ω) that can be equated to $1/R_PC_P$, we could also determine the capacitance (C_P) of the C_P−R_P network (inset of Figure 9).

We also compared the Nyquist plots of devices based on sections of the p−i−n heterojunction, that is, p−i and i−n layers. From the semicircular plots, we found that the bulk resistance (R_P) of the p−i−n device was expectedly higher than that of both p−i and i−n devices. Since the p−i−n heterojunction contained two depletion regions at the p−i and i−n interfaces and the p−i and i−n heterojunctions contained only one such region each, we compared the capacitive component of the complex impedance of the devices. From the frequency at the apex of Nyquist plots, we determined the capacitance of the C_P−R_P combination. We have observed that the capacitance of the p−i−n heterojunction was lower than that of p−i and i−n devices (inset of Figure 9). This implied that in the p−i−n device, the capacitors originating due to the depletion regions at p−i and i−n interfaces were indeed in series combination. In other words, the impedance spectroscopy also inferred that two depletion regions were formed in the p−i−n heterostructure.

CONCLUSION

In conclusion, we have studied photovoltaic properties of $BiFeO_3$ nanoparticles sandwiched between p- and n-type layers forming a p−i−n heterojunction. A thin film of NiO or MoO_3 nanoparticles as a p-type layer and a layer of n-type ZnO nanoparticles were used to form the double-interfaced heterojunction based on all-inorganic oxide, nontoxic, and perovskite materials. From STM measurements and corresponding DOS spectra, we determined conduction and valence band edges of the materials in order to draw an energy level diagram of the p−i−n heterojunction. The energy levels with type-II band alignment at the two junctions favored carrier separation at the p−i and i−n interfaces of the p−i−n heterojunction. Current−voltage characteristics of the p−i−n heterojunction, along with that of single interfaces in the form of p−i and i−n junctions, sandwiched between two electrodes, were recorded under dark and white light illuminated conditions. Results showed that the photovoltaic properties improved due to two depletion regions formed at the p−i and i−n interfaces of p−i−n heterojunctions.

ASSOCIATED CONTENT

Supporting Information

Detailed description of the growth and characterization of MoO_3 nanoparticles, thin films of NiO, and ZnO nanoparticles (Figures S1−S3), SEM image of a p−i−n heterojunction (Figure S4), surface profile of a couple of thin films imaged with an AFM (Figure S5), and EQE spectrum of MoO_3−$BiFeO_3$−ZnO (p−i−n) heterojunction sandwiched between ITO and aluminum electrodes and an optical absorption spectrum of the p−i−n heterojunction (Figure S6). This material is available free of charge via the Internet at http://pubs.acs.org.

AUTHOR INFORMATION

Corresponding Author

*Tel: +91-33-24734971. Fax: +91-33-24732805. E-mail: sspajp@iacs.res.in.

Notes

The authors declare no competing financial interest.

ACKNOWLEDGMENTS

S.C. acknowledges DST Inspire Fellowship (IF 140158). A.B. acknowledges CSIR Fellowship No. 09/080(0779)/2011-EMR-I (Roll No. 510847). The authors acknowledge financial assistance from DeitY, SERIIUS, and Nano Mission (DST) projects.

REFERENCES

(1) Lincot, D.; Guillemoles, J. F.; Taunier, S.; Guimard, D.; Sicx-Kurdi, J.; Chaumont, A.; Roussel, O.; Ramdani, O.; Hubert, C.; Fauvarque, J. P.; Bodereau, N.; Parissi, L.; Panheleux, P.; Fanouillere, P.; Naghavi, N.; Grand, P. P.; Benfarah, M.; Mogensen, P.; Kerrec, O. Chalcopyrite Thin Film Solar Cells by Electrodeposition. *Sol. Energy* **2004**, *77*, 725−737.

(2) Redinger, A.; Berg, D. M.; Dale, P. J.; Siebentritt, S. The Consequences of Kesterite Equilibria for Efficient Solar Cells. *J. Am. Chem. Soc.* **2011**, *133*, 3320−3323.

(3) Mitzi, D. B.; Gunawan, O.; Todorov, T. K.; Wang, K.; Guha, S. The Path towards a High-Performance Solution-Processed Kesterite Solar Cell. *Sol. Energy Mater. Sol. Cells* **2011**, *95*, 1421−1436.

(4) Jasieniak, J.; MacDonald, B. I.; Watkins, S. E.; Mulvaney, P. Solution-Processed Sintered Nanocrystal Solar Cells via Layer-by-Layer Assembly. *Nano Lett.* **2011**, *11*, 2856−2864.
(5) Krishnakumar, V.; Barati, A.; Schimper, H. J.; Klein, A.; Jaegermann, W. A Possible Way To Reduce Absorber Layer Thickness in Thin Film CdTe Solar Cells. *Thin Solid Films* **2013**, *535*, 233−236.
(6) Dasgupta, U.; Saha, S. K.; Pal, A. J. Fully-Depleted *pn*-Junction Solar Cells Based on Layers of Cu_2ZnSnS_4 (CZTS) and Copper-Diffused $AgInS_2$ Ternary Nanocrystals. *Sol. Energy Mater. Sol. Cells* **2014**, *124*, 79−85.
(7) Ko, D.-K.; Brown, P. R.; Bawendi, M. G.; Bulovic, V. p-i-n Heterojunction Solar Cells with a Colloidal Quantum-Dot Absorber Layer. *Adv. Mater.* **2014**, *26*, 4845−4850.
(8) Rath, A. K.; Bernechea, M.; Martinez, L.; Konstantatos, G. Solution-Processed Heterojunction Solar Cells Based on p-Type PbS Quantum Dots and n-Type Bi_2S_3 Nanocrystals. *Adv. Mater.* **2011**, *23*, 3712−3717.
(9) Chang, L.-Y.; Lunt, R. R.; Brown, P. R.; Bulovic, V.; Bawendi, M. G. Low-Temperature Solution-Processed Solar Cells Based on PbS Colloidal Quantum Dot/CdS Heterojunctions. *Nano Lett.* **2013**, *13*, 994−999.
(10) Luther, J. M.; Law, M.; Beard, M. C.; Song, Q.; Reese, M. O.; Ellingson, R. J.; Nozik, A. J. Schottky Solar Cells Based on Colloidal Nanocrystal Films. *Nano Lett.* **2008**, *8*, 3488−3492.
(11) Green, M. A.; Ho-Baillie, A.; Snaith, H. J. The Emergence of Perovskite Solar Cells. *Nat. Photonics* **2014**, *8*, 506−514.
(12) Huang, H. Solar Energy: Ferroelectric Photovoltaics. *Nat. Photonics* **2010**, *4*, 134−135.
(13) Snaith, H. J. Perovskites: The Emergence of a New Era for Low-Cost, High-Efficiency Solar Cells. *J. Phys. Chem. Lett.* **2013**, *4*, 3623−3630.
(14) Hao, F.; Stoumpos, C. C.; Duyen Hanh, C.; Chang, R. P. H.; Kanatzidis, M. G. Lead-Free Solid-State Organic−Inorganic Halide Perovskite Solar Cells. *Nat. Photonics* **2014**, *8*, 489−494.
(15) Lee, M. M.; Teuscher, J.; Miyasaka, T.; Murakami, T. N.; Snaith, H. J. Efficient Hybrid Solar Cells Based on Meso-Superstructured Organometal Halide Perovskites. *Science* **2012**, *338*, 643−647.
(16) Xing, G.; Mathews, N.; Sun, S.; Lim, S. S.; Lam, Y. M.; Graetzel, M.; Mhaisalkar, S.; Sum, T. C. Long-Range Balanced Electron- and Hole-Transport Lengths in Organic−Inorganic $CH_3NH_3PbI_3$. *Science* **2013**, *342*, 344−347.
(17) Burschka, J.; Pellet, N.; Moon, S.-J.; Humphry-Baker, R.; Gao, P.; Nazeeruddin, M. K.; Graetzel, M. Sequential Deposition as a Route to High-Performance Perovskite-Sensitized Solar Cells. *Nature* **2013**, *499*, 316−319.
(18) Wang, J.; Neaton, J. B.; Zheng, H.; Nagarajan, V.; Ogale, S. B.; Liu, B.; Viehland, D.; Vaithyanathan, V.; Schlom, D. G.; Waghmare, U. V.; Spaldin, N. A.; Rabe, K. M.; Wuttig, M.; Ramesh, R. Epitaxial $BiFeO_3$ Multiferroic Thin Film Heterostructures. *Science* **2003**, *299*, 1719−1722.
(19) Khan, G. G.; Das, R.; Mukherjee, N.; Mandal, K. Effect of Metal Doping on Highly Efficient Photovoltaics and Switchable Photovoltage in Bismuth Ferrite Nanotubes. *Phys. Status Solidi RRL* **2012**, *6*, 312−314.
(20) Seidel, J.; Fu, D.; Yang, S.-Y.; Alarcon-Llado, E.; Wu, J.; Ramesh, R.; Ager, J. W., III Efficient Photovoltaic Current Generation at Ferroelectric Domain Walls. *Phys. Rev. Lett.* **2011**, *107*, 126805.
(21) Choi, T.; Lee, S.; Choi, Y. J.; Kiryukhin, V.; Cheong, S. W. Switchable Ferroelectric Diode and Photovoltaic Effect in $BiFeO_3$. *Science* **2009**, *324*, 63−66.
(22) Yang, S. Y.; Seidel, J.; Byrnes, S. J.; Shafer, P.; Yang, C. H.; Rossell, M. D.; Yu, P.; Chu, Y. H.; Scott, J. F.; Ager, J. W., III; Martin, L. W.; Ramesh, R. Above-Bandgap Voltages from Ferroelectric Photovoltaic Devices. *Nat. Nanotechnol.* **2010**, *5*, 143−147.
(23) Chen, B.; Li, M.; Liu, Y.; Zuo, Z.; Zhuge, F.; Zhan, Q.-F.; Li, R.-W. Effect of Top Electrodes on Photovoltaic Properties of Polycrystalline $BiFeO_3$ Based Thin Film Capacitors. *Nanotechnology* **2011**, *22*, 195201.
(24) Qu, T. L.; Zhao, Y. G.; Xie, D.; Shi, J. P.; Chen, Q. P.; Ren, T. L. Resistance Switching and White-Light Photovoltaic Effects in $BiFeO_3$/Nb-$SrTiO_3$ Heterojunctions. *Appl. Phys. Lett.* **2011**, *98*, 173507.
(25) Jo, S.-H.; Lee, S.-G.; Lee, Y.-H. Ferroelectric Properties of PZT/BFO Multilayer Thin Films Prepared Using the Sol−Gel Method. *Nanoscale Res. Lett.* **2012**, *7*, 54.
(26) Tu, C. S.; Hung, C. M.; Xu, Z. R.; Schmidt, V. H.; Ting, Y.; Chien, R. R.; Peng, Y. T.; Anthoninappen, J. Calcium-Doping Effects on Photovoltaic Response and Structure in Multiferroic $BiFeO_3$ Ceramics. *J. Appl. Phys.* **2013**, *114*, 124105.
(27) Liu, Z.; Yan, F. Photovoltaic Effect of $BiFeO_3$/Poly(3-hexylthiophene) Heterojunction. *Phys. Status Solidi RRL* **2011**, *5*, 367−369.
(28) Park, T.-J.; Papaefthymiou, G. C.; Viescas, A. J.; Moodenbaugh, A. R.; Wong, S. S. Size-Dependent Magnetic Properties of Single-Crystalline Multiferroic $BiFeO_3$ Nanoparticles. *Nano Lett.* **2007**, *7*, 766−772.
(29) Bhaumik, S.; Pal, A. J. Light-Emitting Diodes Based on Solution-Processed Nontoxic Quantum Dots: Oxides as Carrier-Transport Layers and Introducing Molybdenum Oxide Nanoparticles as a Hole-Inject Layer. *ACS Appl. Mater. Interfaces* **2014**, *6*, 11348−11356.
(30) Liu, D.; Kelly, T. L. Perovskite Solar Cells with a Planar Heterojunction Structure Prepared Using Room-Temperature Solution Processing Techniques. *Nat. Photonics* **2014**, *8*, 133−138.
(31) Mashford, B. S.; Nguyen, T.-L.; Wilson, G. J.; Mulvaney, P. All-Inorganic Quantum-Dot Light-Emitting Devices Formed via Low-Cost, Wet-Chemical Processing. *J. Mater. Chem.* **2010**, *20*, 167−172.
(32) Mocatta, D.; Cohen, G.; Schattner, J.; Millo, O.; Rabani, E.; Banin, U. Heavily Doped Semiconductor Nanocrystal Quantum Dots. *Science* **2011**, *332*, 77−81.
(33) Gao, F.; Yuan, Y.; Wang, K. F.; Chen, X. Y.; Chen, F.; Liu, J. M. Preparation and Photoabsorption Characterization of $BiFeO_3$ Nanowires. *Appl. Phys. Lett.* **2006**, *89*, 102506.
(34) Kothari, D.; Reddy, V. R.; Sathe, V. G.; Gupta, A.; Banerjee, A.; Awasthi, A. M. Raman Scattering Study of Polycrystalline Magnetoelectric $BiFeO_3$. *J. Magn. Magn. Mater.* **2008**, *320*, 548−552.
(35) Pandit, P.; Satapathy, S.; Gupta, P. K.; Sathe, V. G. Effect of Coalesce Doping of Nd and La on Structure, Dielectric, and Magnetic Properties of $BiFeO_3$. *J. Appl. Phys.* **2009**, *106*, 114105.
(36) Das, R.; Sarkar, T.; Mandal, K. Multiferroic Properties of Ba^{2+} and Gd^{3+} Co-Doped Bismuth Ferrite: Magnetic, Ferroelectric and Impedance Spectroscopic Analysis. *J. Phys. D: Appl. Phys.* **2012**, *45*, 455002.
(37) Fang, L.; Liu, J. A.; Ju, S.; Zheng, F. G.; Dong, W.; Shen, M. R. Experimental and Theoretical Evidence of Enhanced Ferromagnetism in Sonochemical Synthesized $BiFeO_3$ Nanoparticles. *Appl. Phys. Lett.* **2010**, *97*, 242501.
(38) Das, R.; Khan, G. G.; Varma, S.; Mukherjee, G. D.; Mandal, K. Effect of Quantum Confinement on Optical and Magnetic Properties of Pr-Cr-Codoped Bismuth Ferrite Nanowires. *J. Phys. Chem. C* **2013**, *117*, 20209−20216.
(39) Zang, Y.; Xie, D.; Wu, X.; Chen, Y.; Lin, Y.; Li, M.; Tian, H.; Li, X.; Li, Z.; Zhu, H.; Ren, T.; Plant, D. Enhanced Photovoltaic Properties in Graphene/Polycrystalline $BiFeO_3$/Pt Heterojunction Structure. *Appl. Phys. Lett.* **2011**, *99*.
(40) Dong, W.; Guo, Y.; Guo, B.; Li, H.; Liu, H.; Joel, T. W. Enhanced Photovoltaic Effect in $BiVO_4$ Semiconductor by Incorporation with an Ultrathin $BiFeO_3$ Ferroelectric Layer. *ACS Appl. Mater. Interfaces* **2013**, *5*, 6925−6929.